Ordering and surface segregation in Co_1 − −cPt_c nanoparticles: A theoretical study from surface alloys to nanoalloys

A. Lopes, G. Tréglia, C. Mottet, B. Legrand

Ordering and surface segregation in $Co_{1-c}Pt_c$ nanoparticles: A theoretical study from surface alloys to nanoalloys

A. Lopes, G. Tréglia, and C. Mottet
Aix Marseille Université, CNRS, CINaM UMR 7325, Campus de Luminy, 13288 Marseille, France

B. Legrand
SRMP-DMN, CEA Saclay, F91191 Gif-sur-Yvette Cedex, France

(Received 18 September 2014; revised manuscript received 26 November 2014; published 9 January 2015)

Monte Carlo simulations within a tight-binding Ising model (TBIM) have been performed on bulk, surfaces, and nanoclusters of Co_{1-c}-Pt_c alloys in order to describe and understand the competition or synergy between surface segregation and chemical ordering phenomena in nanoalloys. Considering effective pair interactions (EPIs) up to the third neighbors, we put in evidence new ordered phases at low temperature in the Co-Pt bulk phase diagram. On the infinite (100) and (111) surfaces, the Pt surface segregation leads to select the Pt-rich plan at the surface without modification of the bulk ordering in the (100) orientation but with an extension of the ordering on a larger composition range in the (111) orientation as compared to the bulk. The truncated octahedron clusters of 405 and 1289 atoms are studied. Their chemical structure is compared in their core with the bulk phase diagram and in their facets with the (111) and (100) infinite surfaces segregation isotherms. The cluster core presents an asymmetry as compared to the bulk phase diagram. The (111) facets are similar to the (111) surface, whereas the (100) facets present geometrical frustrations for the segregation versus core ordering.

DOI: 10.1103/PhysRevB.91.035407 PACS number(s): 71.20.Be, 61.66.Dk, 68.35.bd, 45.70.Mg

I. INTRODUCTION

The study of chemical ordering and surface segregation effects in nanoalloys is crucial in the characterization of their properties and applications [1,2]. "Nanoalloys" currently describe the nanoparticles or nanoclusters including more than one metallic species [3]. In such systems, the surface plays a major role. Except for very small clusters made of less than one hundred of atoms, where almost all the atoms are located at the surface, it is possible to distinguish a surface and a core for other systems with a few hundreds to a few thousands of atoms (a few nanometers in size) to be compared to infinite surface and bulk systems. Bulk alloys [4] and surface alloys [5–13] have been the subject of intensive studies at the end of the twentieth century. We will show now how core ordering and surface segregation in nanoalloys can be compared respectively to bulk phase diagram and alloy surface segregation in order, firstly, to get a better understanding of the nanoalloys structure and secondly, eventually, to describe specific behaviours in nanoalloys which do not exist in other systems.

Co-Pt systems, beginning with surfaces and thin films [14–20] and more recently nanoalloys [21–38], have been studied experimentally for decades because of their specific magnetic and catalytic properties. For example, the effect of the chemical order on the electrocatalytic activity of model PtCo electrodes used in fuel cells has been evident recently [39,40]. Theoretical investigations have been performed on alloy surfaces [7–11], and nanoalloys of Fe-Pt or Co-Pt [41–53]. The studies on nanoparticles have been mostly concentrated on the equiatomic composition, because of the high magnetic anisotropy of the $L1_0$ ordered phase in (Fe,Co)-Pt systems, which is expected to compensate the superparamagnetism of nanoparticles used for the next-generation recording media for ultrahigh density data storage. One crucial question was to characterize the order-disorder transition temperature as a function of the cluster size since theoretical models agree to conclude that it decreases with cluster size [43,44,47,50], which has been experimentally confirmed by high-resolution transmission electron microscopy [33] and by synchrotron $X-$ray diffraction [28]. Moreover, the nature of the transition displays a first order type as in the bulk as shown by the experimental [28] and theoretical [53] evidences of phase coexistence between the ordered and disordered phases even though there is a smoothing with decreasing cluster size [42,44,47,52].

Theoretical studies are rarely devoted to both variable concentrations and temperatures. We have extended the description of bimetallic nanoparticles to the whole concentration range of $Co_{1-c}Pt_c$ alloys and different temperatures in order to draw nanoalloys phase diagrams. This is performed using Monte Carlo simulations in the semigrand canonical ensemble and a tight-binding Ising model where the energetic parameters have been fitted to *ab initio* calculations and semiempirical interatomic potential (TB-SMA: tight-binding - second moment approximation) in order to take into account in an effective way both chemical ordering tendency and atomic structure rearrangements due to lattice mismatch between the two components.

After describing the model and method in Sec. II, the bulk alloy phase diagram issued from our calculations will be presented in Sec. III. Section IV will be devoted to the (111) and (100) alloy surfaces at high and low temperatures, i.e., in the disordered and ordered states. Finally, we will present the results on nanoalloys considering truncated octahedra of 405 and 1289 atoms in the whole composition range in the disordered and ordered states, depending on the temperature, in Sec. V and the conclusions, and perspectives in the last section.

II. MODEL AND METHOD

A. Tight-binding Ising model (TBIM)

In bimetallic alloys, the alloying effect comes from the difference between the atomic d-band levels of the two

components (called the diagonal disorder), and the small part of the energy coming from the chemical configuration can be expressed, on a rigid lattice, in terms of effective pair interactions. This is the tight-binding Ising model (TBIM) [8,54] in which the Hamiltonian writes

$$H^{\mathrm{TBIM}} = \sum_{n,m} p_n p_m V_{nm} + \sum_n p_n \left(\Delta h_n + \Delta h_n^{\mathrm{size}}\right), \qquad (1)$$

where p_n is the occupation factor of one of the species equal to 1 if the site n is occupied by an atom of this species, or 0 if not. V_{nm} is an effective pair interaction (EPI) between the atoms at sites n and m, which determines the chemical preference for hetero- or homoatomic bonds, leading to ordering ($V_{nm} > 0$) or phase separation ($V_{nm} < 0$). In the face centered cubic structure (fcc) it has been shown [55] that first-neighbor interactions V^1 (for sites n and m first-neighbors) dominate as compared to the following V^2, V^3, V^4. Therefore in general, we consider only first-neighbor pairs V^1. However, to stabilize the $L1_0$ phase of CoPt alloy with respect to the A_2B_2 one, it is necessary to go at least to the second-neighbor EPIs [4,46,47] with $V^2 < 0$.

The second term of Eq. (1) corresponds to a local contribution to the energy induced by inequivalent geometrical environments in inhomogeneous systems like surfaces or clusters. It is composed of a cohesive term (Δh_n) and a relaxation term ($\Delta h_n^{\mathrm{size}}$) due to size mismatch between the two elements. They are nonzero for sites n, which belong to the surface written Δh and Δh^{size} in the following. Δh is equal to the difference of the site excess energies of the two elements (favoring the element with the lowest one to segregate). Δh^{size} is calculated within a many-body interatomic potential (TB-SMA) where an impurity differs from the matrix only by its atomic radius.

As a consequence, the TBIM presents three phenomenological effects to control the surface segregation: the alloying effect, which favours the segregation of the minority element when $V < 0$, or the majority element with an oscillating profile when $V > 0$; the cohesive effect (Δh), which promotes the segregation of the element with the lowest cohesive energy; and the size effect (Δh^{size}), which promotes the minority atom when it is the biggest one.

B. Co-Pt TBIM parameters

Even though the TBIM parameters could be directly calculated from the electronic structure of the disordered system, we have chosen here to derive them from total energy calculations performed either by first-principles calculations, semiempirical many-body interatomic potentials (TB-SMA) and from the experimental transition temperatures of the bulk phase diagram [56].

The first-principles calculations are performed within the density functional theory (DFT) using the VASP code with the generalized gradient approximation (GGA) [57] and the projector augmented wave (PAW) [58,59] interaction potential between the ions and the electrons. The s and d valence electrons are considered for each metal with a cutoff energy equal to 600 eV for plane wave basis set. The Brillouin zone integration is performed with the Monkhorst-Pack scheme with k-point mesh comprising 12 to 19 subdivisions along each reciprocal lattice vector. The cohesive energy, lattice parameter, and surface energies have been calculated for Co and Pt, using spin-polarized calculations for Co (see the results in Table I).

TABLE I. DFT and TB-SMA calculations of the lattice parameters, cohesive energy and surface energies of the pure metals. Experimental values are taken from Kittel (Wiley, New York, 1996) and Simmons and Wang (MIT, Cambridge, 1971).

	a (Å)	E_{coh} (eV/at.)	$\gamma^{(111)}$	$\gamma^{(100)}$ (eV/at.)/(mJ/m^2)	$\gamma^{(110)}$
Co					
DFT	3.52	−5.35	0.68/2030	0.96/2470	1.31/2400
TB-SMA	3.52	−5.35	0.78/2330	0.94/2425	1.39/2540
Exp.	3.54	−4.45		1.00/2590	
Pt					
DFT	3.98	−5.53	0.64/1500	0.91/1850	1.31/1870
TB-SMA	3.98	−5.53	0.68/1590	0.85/1720	1.30/1860
Exp.	3.92	−5.86		1.19/2480	

We also use a semiempirical potential derived from the second moment approximation of the density of states in a tight-binding model (TB-SMA) [60] to complete the fitting procedure. This potential has been fitted both to DFT calculations (Table I) and to the experimental Co-Pt bulk phase diagram [56,61–63], especially to respect the experimental order/disorder transition temperatures which results in overestimated and asymmetric mixing enthalpies in the tight binding model as compared to the *ab initio* values (see the corresponding mixing enthalpies Fig. 1). This is a new version as compared to the one used in previous studies [50,53] where only the order/disorder transition at equiconcentration was investigated.

There are three different TBIM parameters to be fitted: the EPIs, V, the cohesive effect, Δh, and the size effect, Δh^{size}. The EPIs have been fitted both on *ab initio* and TB-SMA potential up to the third-neighbor interactions by calculating the

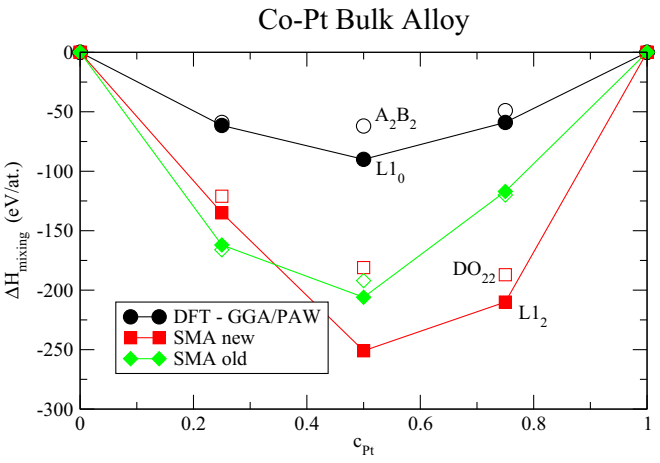

FIG. 1. (Color online) Mixing enthalpies of the bulk Co-Pt alloys at stoichiometries Co_3Pt, CoPt, and $CoPt_3$ with the DFT calculations (black circles), TB-SMA used in this study (red squares) or an other parametrization [50,53] (green diamonds). Full symbols represent the $L1_0$ and $L1_2$ phases, whereas empty symbols represent the DO_{22} and A_2B_2 phases.

energy difference between isolated and near-neighbor impurities, taking into account atomic relaxations. The reason for going to third neighbors is that we find positive values for V^1 and V^2 both by DFT and TB-SMA calculations. Therefore V^3 must be positive to stabilize the $L1_0$ phase with respect to the A_2B_2 one [4] given the expressions of the mixing enthalpies per atom of these phases as $\Delta E_{L1_0} = -4V^1 + 0V^2 - 8V^3(+0V^4 + \cdots)$, $\Delta E_{A_2B_2} = -4V^1 - V^2 - 4V^3(-4V^4 + \cdots)$, $\Delta E_{L1_2} = -3V^1 + 0V^2 - 6V^3(+0V^4 + \cdots)$, and $\Delta E_{DO_{22}} = -3V^1 - \frac{1}{2}V^2 - 4V^3(-2V^4 + \cdots)$.

TB-SMA calculations give a positive value for V^3, in agreement with a cluster expansion study fitted to *ab initio* calculations [52] where the EPIs vanished only beyond the fourth-neighbor distance. We get the values: $V^1 = 69$ meV, $V^2 = 16$ meV, and $V^3 = 16$ meV.

Concerning the cohesive effect for surface segregation, we can notice that the Pt surface energy calculated by DFT is lower than the one of Co, which is in favor of the Pt surface segregation, as already obtained by Dannenberg *et al.* [64]. However, experimentally, the difference in surface energies is very small and, as a consequence, their difference changes of sign as it is expressed in eV/at. or in mJ/m^2 because of the difference in lattice parameter between Co and Pt. The parameter Δh, which is equal to the difference in surface excess energy between Pt and Co, will be fixed to -0.10 eV (in favor of the Pt segregation) for each surface site, which also fits with the TB-SMA differences of excess energy for the edge and vertex of truncated octahedron (TOh) clusters between Co and Pt, which are equal to -0.11 and -0.10 eV, respectively.

Finally, the Δh^{size} parameters taking into account, on an effective lattice, the difference in size of the two elements, are calculated via the segregation energies using a quenched molecular dynamic simulation and the TB-SMA potential where the impurity differs from the matrix only by its atomic radius. The values of Δh^{size} are given in Table II for the two diluted alloys and different surface sites of a TOh cluster of 1289 atoms. Whereas in the Co impurity case [Pt(Co)] the size effect increases with the number of cutting bonds at the cluster surface towards a weak Co segregation, the size effect is not monotonic in the Pt impurity (which is the largest atom) being the highest for the (100) facet in favor of Pt segregation. The reason of such an effect comes from the atomic contraction of the distances in the low coordinated sites (edge and vertex) leading to a weakening of the Pt segregation at low coordinated sites. Similar result has been obtained in the Cu(Ag) system [65]. We use a linear extrapolation for different concentrations between the two diluted limits.

TABLE II. TBIM Δh^{size} parameters obtained by TB-SMA calculations of the segregation energies of one impurity differing from its matrix only by its atomic radius for a Pt impurity in Co matrix: Co(Pt) or a Co impurity in Pt matrix: Pt(Co) and for the different surface sites of a TOh cluster of 1289 atoms. In the TBIM model, we use the Pt concentration as reference so that the Δh^{size} parameters correspond to the segregation energy for Co(Pt) and the opposite value of the segregation energy for Pt(Co).

(in eV)	(111)	(100)	edge	vertex
Co(Pt)	−0.21	−0.45	−0.30	−0.28
Pt(Co)	0.05	0.07	0.11	0.17

C. Monte Carlo simulations

We performed Monte Carlo simulations in canonical and semigrand canonical ensembles. In the first case, the concentration remains constant and the Monte Carlo trials consist in exchanging the positions of two atoms of different nature. In the second case, the difference of the chemical potential of the two elements remains constant, which determines the average concentration. The Monte Carlo trials consist in permuting the chemical nature of one atom. In each case, we keep the same number of atoms in the simulation box.

The Metropolis sampling [66] ensures that we reach a Boltzmann distribution of the chemical configurations at equilibrium, this means the number of Monte Carlo trials is sufficient to get reliable averages of physical quantities. In the Metropolis Monte Carlo, a trial is accepted if it lowers the total energy of the system. If not, it can be still accepted with a probability equal to $\exp(-\frac{\Delta E}{kT})$, where ΔE is the energy difference between the configurations before and after the trial, k is the Boltzmann constant, and T the temperature.

We performed twenty- to forty-thousand macrosteps in each simulation after leaving the system to equilibrate during five- to ten-thousand macrosteps. Each macrostep consists of proposing randomly to any atom of the box a Monte Carlo trial (exchange or permutation), repeated as many times as there are atoms in the box.

For the canonical simulations, we performed either heating and cooling runs starting respectively from low-temperature ordered configurations and high-temperature disordered configurations. Then, at each increment of the temperature, we start with the last configuration. For the semigrand canonical simulations, we started from pure systems, either Co or Pt, and increased or decreased the chemical potential keeping the last configuration as a starting configuration.

D. Order parameters

The face-centered cubic (fcc) lattice constitutes four simple cubic sublattices as illustrated in Fig. 2. The ordered phases are defined by an alternate stacking of pure atomic planes in one direction for the $L1_0$ and pure and mixed atomic planes for the $L1_2$ phase. The A_2B_2 and DO_{22} (Fig. 2) are some

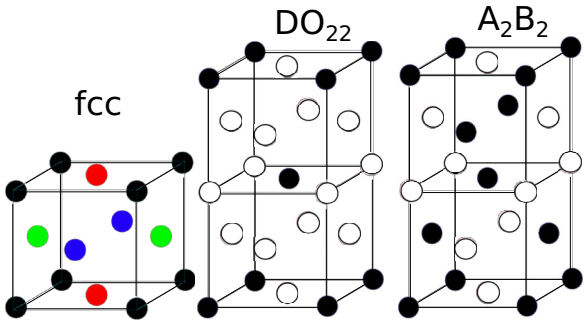

FIG. 2. (Color online) From left to right, the four sublattices in the fcc structure: α (black), β (red), γ (green) and δ (blue), DO_{22}, and A_2B_2 phases.

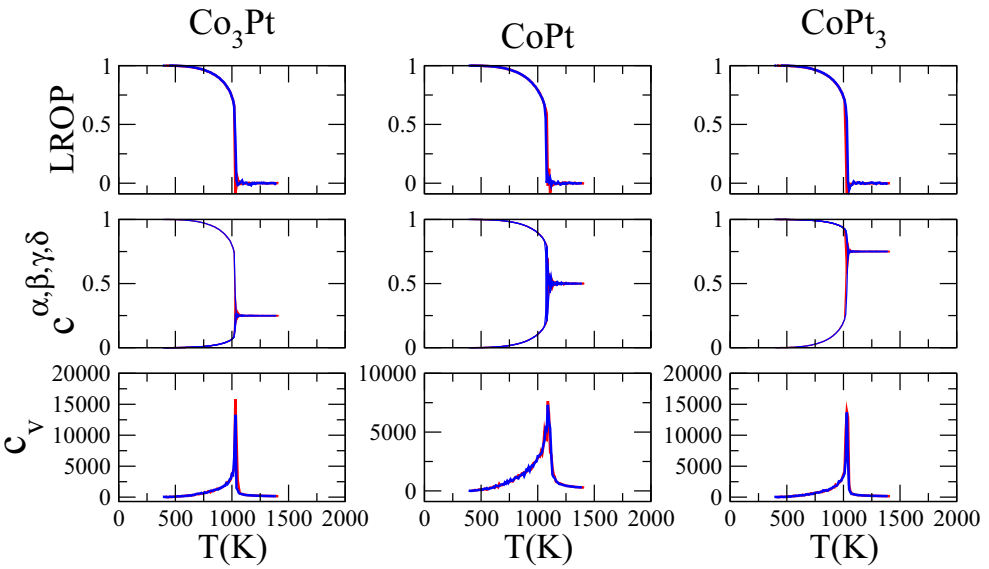

FIG. 3. (Color online) Order/disorder transitions obtained from canonical Monte Carlo simulations for stoichiometric Co_3Pt, CoPt, and $CoPt_3$ alloys. The first line represents the LROP, the second line the sublattice occupation rates, and the third line the calorific capacity. The heating (red) and cooling (blue) curves are quite indistinguishable.

alternatives to these phases, differing by their second-neighbor interactions.

The long-range-order parameter (LROP) is defined as a function of the Pt concentration on each sublattice written c^α, c^β, c^γ, and c^δ. The LROP are then characterized for the Co_3Pt ($L1_2$), CoPt ($L1_0$), and $CoPt_3$ ($L1_2$) phases by the following expressions:

$$\mathrm{LROP}(Co_3Pt) = \tfrac{1}{3}(c^\alpha + 2) - (c^\beta + c^\gamma + c^\delta), \quad (2)$$

$$\mathrm{LROP}(CoPt) = \tfrac{1}{2}(c^\alpha + c^\beta - c^\gamma - c^\delta), \quad (3)$$

$$\mathrm{LROP}(CoPt_3) = c^\alpha + c^\beta + c^\gamma - \frac{c^\delta}{3} - 2, \quad (4)$$

where the sublattices are filled successively following the order $c^\alpha > c^\beta > c^\gamma > c^\delta$.

To distinguish between the $L1_0/A_2B_2$ and the $L1_2/DO_{22}$ in terms of LROP, it would be necessary to extend the number of sublattices. Here, we chose to use the short-range-order parameter (SROP) defined by Cowley [67] following the expression

$$\alpha^n = 1 - \frac{P^n_{AB}}{c(1-c)} = 1 - \frac{p^n_{AB}}{1-c}, \quad (5)$$

where P^n_{AB} is the probability to find an atom of type A n^{th} neighbor of an atom of type B. This probability is equal to the probability to find an atom of type B (equal to the concentration in B noted "c") multiplied by the probability to find a mixed pair n^{th} neighbor of this atom, noted p^n_{AB}, equal to the average number of mixed pairs (n^{th} neighbor) normalized by the total number of n^{th} neighbor pairs. This SROP takes defined values depending on the composition and the type of ordered phases as shown in Table III.

TABLE III. SROP at first- and second-neighbor distances: α^1 and α^2 depending on the concentration and the ordered phases.

	α^1	$\alpha^2_{L1_0/L1_2}$	$\alpha^2_{A_2B_2/DO_{22}}$
$c = 0.25$	–1	1	1/3
$c = 0.5$	–1/3	1	1/3
$c = 0.75$	1/3	1	7/9

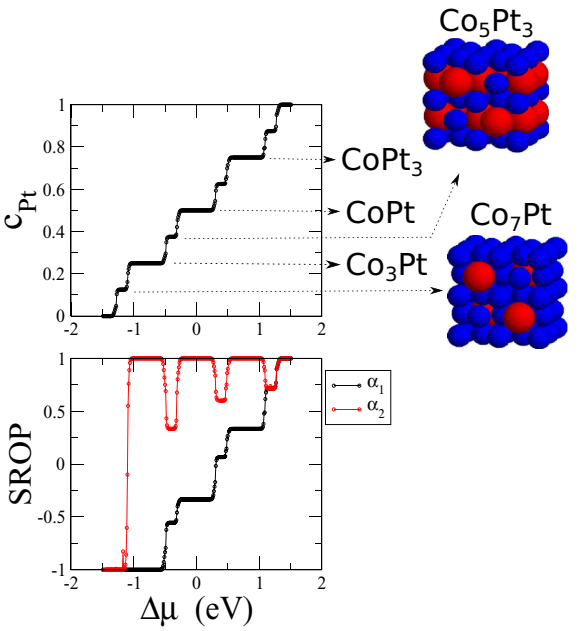

FIG. 4. (Color online) Isotherm of bulk $Co_{1-c}Pt_c$ system at 100 K obtained by semigrand canonical Monte Carlo simulations. The Pt concentration and SROP for the first (α^1) and second neighbors (α^2) are plotted as a function of the chemical potential difference $\Delta\mu = \mu_{Pt} - \mu_{Co}$. The mesh of the compounds Co_7Pt and Co_5Pt_3 are displayed (Co atoms in blue and Pt atoms in red). Co atoms are smaller and in blue, Pt atoms are larger and in red.

III. TBIM Co-Pt BULK PHASE DIAGRAM

The bulk is represented by a cubic box of 2048 atoms (with edge of eight times the lattice parameter) and periodic conditions. The order/disorder critical temperature of the stoichiometric phases has been characterized by canonical simulations, increasing or decreasing the temperature with the aim to increase disorder or order in the system. The results are shown in Fig. 3 where we can see the LROP, the sublattices occupation rates, and the heat capacity $C_V = (\frac{dE}{dT})_V$. We notice that the heating and cooling curves are superimposed so there is no hysteresis phenomenon as it has been observed using the TB-SMA potential and Monte Carlo simulations with atomic displacements [28], even though the transition is abrupt and well defined as a first-order transition. The critical order/disorder temperature at equiconcentration is 1100 K as fitted on the experimental data [56,63]. The $L1_2$ phases have equivalent critical temperature equal to 1030 K, which is in good agreement with the experimental critical temperature of the $CoPt_3$ phase [56,63] but not for the Co_3Pt alloy for which the critical temperature is lower (830 K) [68]. This asymetry cannot be obtained with the present TBIM model mainly because the EPIs does not depend on the concentration.

The description of the full phase diagram is then performed using semigrand canonical Monte Carlo simulations at constant temperature. The isotherm at low temperature (100 K) displays the ground states of the ordered phases as a function of the difference in the chemical potential $\Delta\mu = \mu_{Pt} - \mu_{Co}$ as illustrated on Fig. 4 with different plateaus of the Pt concentration as a function of $\Delta\mu$. The three larger plateaus characterize the $L1_2$ and $L1_0$ phases also defined by their SROP. The intermediate phases with smaller plateaus correspond to compositions of 0.125, 0.375, 0.625, and 0.875 or to the compounds: Co_7Pt, Co_5Pt_3, Co_3Pt_5, and $CoPt_7$. These

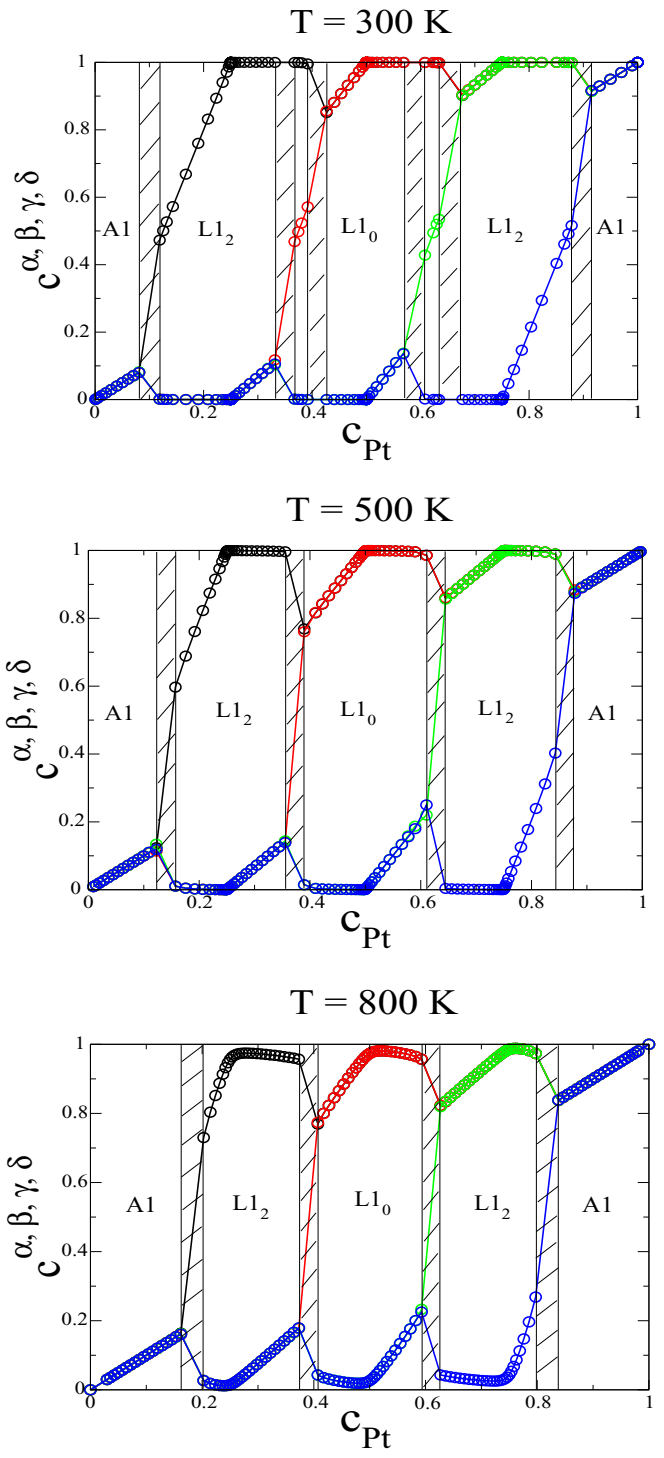

FIG. 5. (Color online) Pt concentrations on the four sublattices as a function of the nominal Pt concentration at 300, 500, and 800 K.

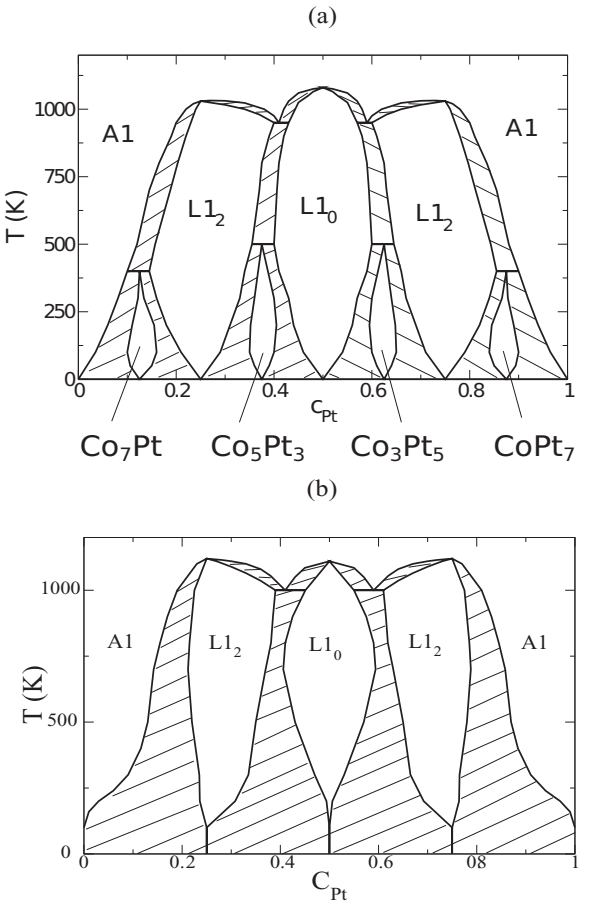

FIG. 6. Bulk phase diagrams: (a) with EPIs up to the third neighbors and (b) with EPIs up to the second neighbors.

phases result in our model from the extension of the EPIs to the third-neighbor interactions and are illustrated in Fig. 4. The isotherms at higher temperature are shown in Fig. 5 where the Pt occupation rates of the four sublattices are plotted as a function of the Pt concentration in the alloy. At low Pt concentration, the four sublattices are equally occupied, which is characteristic of the disordered A_1 phase. Then there is a gap in concentration (the hatched regions) which represents a coexistence domain between the A_1 and the $L1_2$ phase. The $L1_2$ phase is characterized by one sublattice populated with Pt and the three others equally occupied by Co. The next ordered phase by increasing Pt concentration and around the equiconcentration is the $L1_0$ ordered phase, which is characterized by the sublattices equally occupied two by two. Then the isotherms are symmetric in the Pt-rich domain. We can observe the variation of the width of ordered phases and phase coexistence as a function of the temperature. This leads to the bulk phase diagram in Fig. 6(a). As compared to the well known one for $V^1 > 0$ and $V^2 < 0$ [4,69,70] [Fig. 6(b)], we see clearly that the extension to the third neighbors of the EPIs modifies the phase diagram at low temperature. Below 500 K, the domain of the non-stoichiometric ordered phases are enlarged at the expense of the phase-coexistence domains. There are also new ordered phases at intermediate concentrations as mentioned before: $c = 0.125$ (Co_7Pt), 0.375 (Co_5Pt_3), 0.625 (Co_3Pt_5), and 0.875 ($CoPt_7$) due to the third-neighbor positive EPIs.

IV. TBIM Co-P*t* (111) AND (100) SURFACES

A. (111) and (100) surfaces at high temperature in the disordered state

The (111) surface is simulated using a box with atomic (111) planes of 100 atoms, periodic conditions in the x and y directions, and 30 planes in the z direction without periodic condition (3000 atoms). The (100) surface is simulated using (100) atomic planes of 128 atoms and periodic conditions in the x and y directions, and 29 atomic planes in the z directions without periodic condition (3712 atoms). We performed Monte

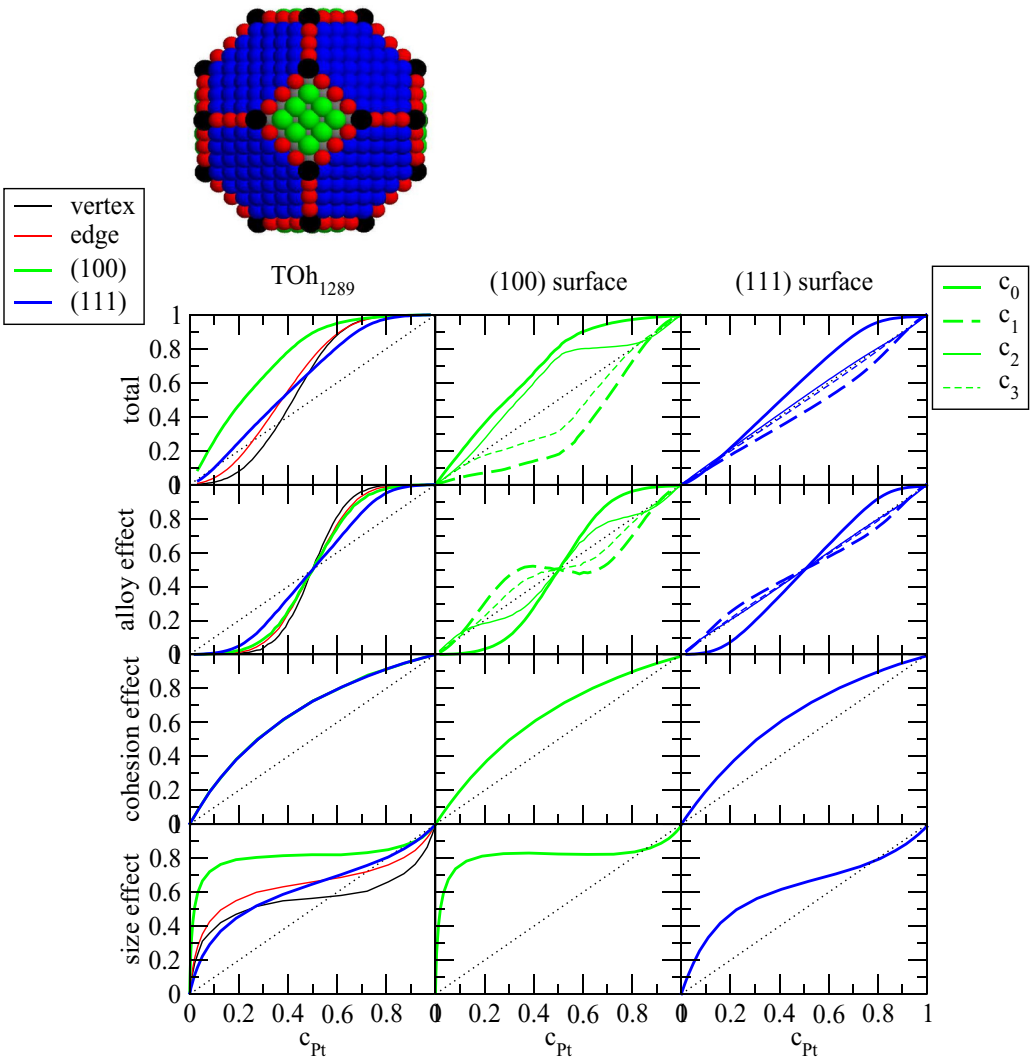

FIG. 7. (Color online) Segregation isotherms at 1200 K for the surface sites (vertex, edge, facets) of a truncated octahedron (TOh) of 1289 atoms of $Co_{1-c}Pt_c$ and for the (100) and (111) infinite surfaces of $Co_{1-c}Pt_c$, and their decomposition concerning, the three driving forces to the segregation: alloying, cohesion, and size effects. In the case of the cluster, the c_{Pt} concentration is the concentration of Pt in the core of the cluster to get a better comparison with the infinite surfaces.

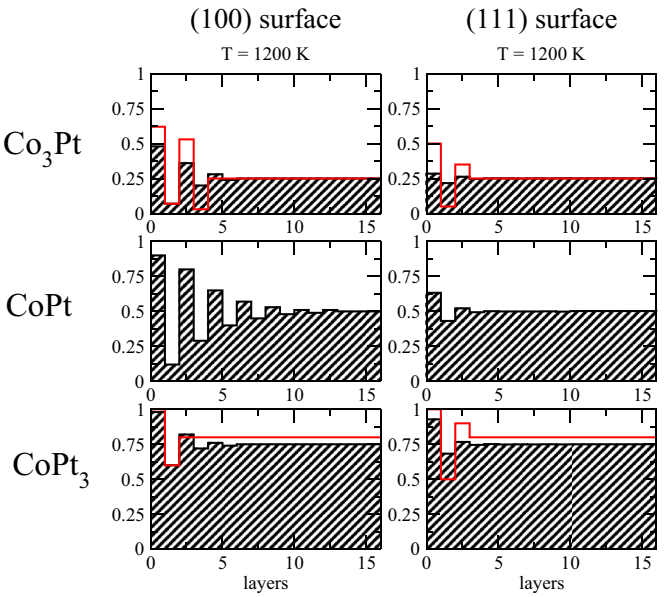

FIG. 8. (Color online) (100) and (111) surface profiles at 1200 K of Co_3Pt, CoPt, and $CoPt_3$. The experimental results are drawn in red: $Co_3Pt(100)$ (Gauthier *et al.* [18]), $CoPt_3(100)$ (Bardi *et al.* [14,15]), $Co_3Pt(111)$ (Gauthier *et al.* [17]), and $CoPt_3(111)$ (Gauthier *et al.* [16]). The experiments are generally performed on disordered single crystals at room temperature.

Carlo simulations in the semigrand canonical ensemble giving segregation isotherms (Pt surface concentration) as a function of the bulk Pt concentration. At a temperature of 1200 K, above order/disorder temperature, the systems are disordered and we follow the concentrations per atomic plane. Starting from the surface, the first four concentrations have been plotted for the (111) and (100) surfaces in Fig. 7. For both surfaces, we notice a Pt surface segregation, stronger in the (100) surface than in the (111), and an oscillating profile, as expected for systems with an ordering tendency. This is in good agreement with the experimental studies [14–18]. The oscillating segregation profiles are displayed in Fig. 8 to better compare with experimental results.

Figure 7 shows also the decomposition of the segregation isotherms in terms of the three driving forces for surface segregation. The alloying effect, namely, the effect of the EPIs, leads to the segregation of the majority species and the amplitude of the segregation is proportional to the number of cutting bonds. The cohesion effect, which is the same for the two surfaces, contributes to the Pt segregation at the surface and concerns only the surface plane (c_0) as the size effect. This last effect promotes the Pt segregation on a large range of concentrations, except in Pt-rich alloys where there is almost no segregation induced by the size effect. The size effect and cohesion effect are sufficient to offset the ordering effect in the Co-rich domain leading to almost no surface segregation in the (111) surface and a slight Pt surface segregation on the (100) surface in this composition domain. In the Pt-rich domain, almost all the driving forces (except the size effect in the diluted domain) lead to Pt surface segregation and the alloying effect seems predominant over the other effects.

B. (100) and (111) surfaces at low temperature in the ordered state

The segregation isotherm at 300 K of the (100) surface is plotted in Fig. 9. The system is ordered as can be checked by the sublattices occupations [Fig. 9(b)], which are similar to that of the bulk 300 K isotherm (Fig. 5). The ordered structures present a stacking of pure or mixed planes, parallel to the (100) surface, so that we can distinguish the α, β sublattices on the even layers $c_{2p}^{\alpha,\beta}$ [Fig. 9(c)] and the γ, δ sublattices on the odd layers $c_{2p+1}^{\gamma,\delta}$ [Fig. 9(d)] across the slab starting with the index 0 at the surface layer. This implies the following relations between the surface concentration and the sublattice concentration:

$$c_{2p}^{(100)} = \tfrac{1}{2}\left(c_{2p}^{\alpha} + c_{2p}^{\beta}\right), \quad c_{2p+1}^{(100)} = \tfrac{1}{2}\left(c_{2p+1}^{\gamma} + c_{2p+1}^{\delta}\right). \qquad (6)$$

First of all, we notice that all the sublattices per layer in the slab are equally occupied except the surface and subsurface ones. Then we notice in Fig. 9(c) that the surface sublattices c_0^{α} and c_0^{β} are almost equivalent to the underneath layers, except small disparities in the disordered Co-rich phase and in the overstoichiometric $L1_2$ Co_3Pt phase where the surface is a little enriched in Pt as compared to the bulk as demonstrated by the slight discrepancies between the c_0^{β} and the c_{2p}^{β} curves. Concerning the subsurface sublattice c_1^{γ} and c_1^{δ} as compared to the c_{2p+1}^{γ} and c_{2p+1}^{δ} ones across the slab, we notice also that the subsurface sublattices are slightly differently occupied with a slight Co subsurface segregation in the c_1^{γ} for the understoichiometric $L1_2$ $CoPt_3$ phase and a slight Pt subsurface enrichment in the c_1^{δ} sublattice for the overstoichiometric $L1_2$ $CoPt_3$ phase.

The surface composition [Fig. 9(a)] along the whole composition range follows the surface sublattice concentration, averaging the c_0^{α} and c_0^{β} for the c_0 surface and the c_1^{γ} and c_1^{δ} for the c_1 subsurface composition, and so on for c_2 and c_3, as expessed by Eq. (6). There is not really a Pt surface segregation but rather the simple manifestation at the surface of the ordered structures of the bulk phase diagram. In the disordered A1 phases, the Pt surface segregation follows qualitatively the one of the high-temperature isotherms (Fig. 7) but with an amplification effect due to the lower temperature. The two surface sublattices are equally occupied by Pt atoms and significantly beyond the bulk Pt composition.

If we consider now each of the bulk ordered phases, we can make the following remarks.

(1) For the Co_3Pt phase, we observe a stacking of mixed and pure Co layers, with a mixed surface, the $c(2\times2)$ ordered surface structure, which has been observed experimentally by low-energy electron diffraction (LEED) and scanning tunneling microscopy (STM) [18]. The experimental superstructure is even more complex since it presents close-packed rows shifted by half the interatomic distance, leading to (1×5), (1×6), and (1×7) patterns between which the $c(2\times2)$ surface phase takes place. The rigid lattice model used here is certainly too simple to reproduce the $(1\times n)$ rows where the local atomic rearrangement is probably due to lattice strain.

(2) From the Co_3Pt to the CoPt phase, the surface Pt concentration accommodates the stoichiometry variation between the two phases following the c_{2p}^{β} sublattice variation

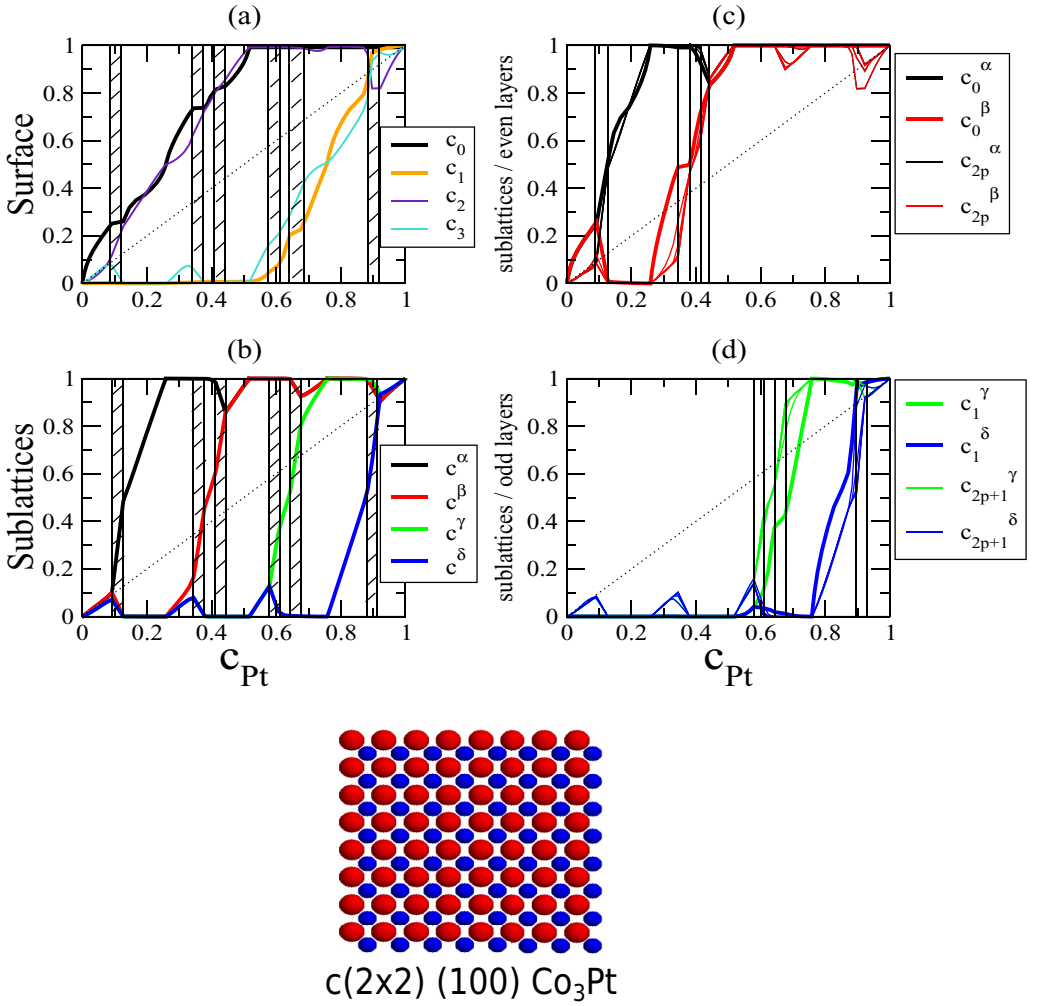

FIG. 9. (Color online) Segregation isotherm at 300 K for the (100) surface. In (a), the surface (c_0) and next planes (c_1, c_2, and c_3) Pt compositions. In (b), the sublattice occupations in the whole slab. On the right, the sublattice concentrations for each layer parallel to the surface $c_p^{\alpha,\beta,\gamma,\delta}$ splitted between the even (graph (c)) and odd layers (d). The hatched areas correspond to the forbidden areas (phase coexistence), which means there are no Monte Carlo points in these areas but we plotted a continuous line for better visibility. The $c(2\times2)(100)$ surface ordered structure is illustrated in the bottom with Co atoms (in blue) and Pt atoms (in red). Co atoms are smaller and in blue, Pt atoms are larger and in red.

with a slightly Pt surface enrichment as compared c_0^{β} to c_{2p}^{β}. More precisely, the slight surface enrichment concerns only the overstoichiometric Co_3Pt phase. Then, there is no more difference between the surface and the bulk β sublattice starting from the Co_5Pt_3 to the CoPt phase.

(3) For the CoPt phase, we observe an alternate stacking of pure planes with a Pt termination at the surface. For the understoichiometric CoPt phase, the surface Pt concentration evolves strictly as the c_{2p}^{β} sublattice.

(4) From the CoPt to the $CoPt_3$ phase, the surface remains Pt pure and the subsurface begins to be filled in Pt following the c_{2p+1}^{γ} sublattice. Here again, the subsurface occupation varies slightly as compared to the bulk ones resulting in a weak Co subsurface enrichment, following the same tendency in the Co_3Pt_5 phase.

(5) For the $CoPt_3$ phase, the surface is naturally pure in Pt and at the stoichiometry, the alloy is ordered with the $L1_2$ phase up to the surface. Out of the stoichiometry, we observe a slight Co enrichment of the subsurface for the understoichiometric alloy and a slight Pt enrichment at the subsurface for the overstoichiometric alloy before to recover the $L1_2$ phase.

As a conclusion, at low temperature, the (100) orientation presents schematically two remarkable segregation profiles, depending on the composition of the alloy relatively to the CoPt equiconcentration. For the Co-rich alloys, the surface is composed of a mixed plane with stoichiometry variations according to the alloy stoichiometry and the first subsurface plane is almost Co-pure. For Pt-rich alloys, the surface is Pt pure and the first subsurface plane is mixed with stoichiometry variations according to the alloy stoichiometry.

Now we consider the segregation isotherms at 500 K for the (111) surface as plotted in Fig. 10. We have chosen this temperature to avoid the Co_5Pt_3 and Co_3Pt_5 ordered phases, which could complicate the description, without bringing important results. In the (111) orientation, each plane parallel

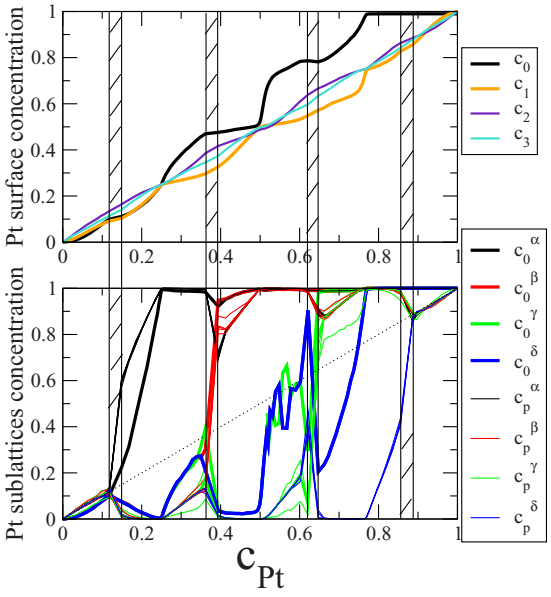

FIG. 10. (Color online) Segregation isotherms at 500 K for the (111) surface with the surface (c_0) and next planes (c_1, c_2, and c_3) Pt compositions, and the sublattice concentrations for each layer parallel to the surface $c_p^{\alpha,\beta,\gamma,\delta}$. The surface sublattices $c_0^{\alpha,\beta,\gamma,\delta}$ are highlighted by thick lines. As in Fig. 9, the hatched areas correspond to the forbidden areas (phase coexistence), which means there are no Monte Carlo points in these areas but we plotted a continuous line for better visibility. Different (111) surface ordered structures are illustrated in the bottom with Co atoms (in blue) and Pt atoms (in red). Co atoms are smaller and in blue, Pt atoms are larger and in red.

to the surface contains the four bulk sublattices (α, β, γ and δ) (as defined in Fig. 2), which was not the case for the (100) surface where each (100) plane contained two bulk sublattices so that two (100) planes were needed to characterize the bulk mesh. The composition of each plane parallel to the (111) surface is then an average of the four layer sublattices so that

$$c_p^{(111)} = \tfrac{1}{4}\left(c_p^{\alpha} + c_p^{\beta} + c_p^{\gamma} + c_p^{\delta}\right). \quad (7)$$

In Fig. 10, starting with low Pt concentration, we observe a linear variation of the surface concentration corresponding to the variation of the composition of the disordered A1 phase, which extends up to the $L1_2$ Co_3Pt ordered phase. Then, the α sublattice begins to be filled first in the bulk and then on the surface so that we observe a slight Co surface enrichment whereas there is almost no segregation at high temperature and same composition. At $c = 0.25$ and beyond, the α sublattice is filled by Pt atoms, whereas the other are equally filled with Co atoms leading to the $c(2\times2)(111)$ surface structure which corresponds to any layer of the $L1_2$ Co_3Pt bulk structure. For overstoichiometric $L1_2$ alloys, the $c_0^{\beta,\gamma,\delta}$ sublattices are equally enriched in Pt, increasing smoothly the c_0 curves up to the equiconcentration, which is almost reached near the phase coexistence domain between the $L1_2$ and the $L1_0$ phases. Then the β sublattice becomes to be filled with Pt, whereas the other γ and δ remain equally Co rich. This corresponds to the first plateau on the segregation isotherm with the $(2\times1)(111)$ surface structure on the $L1_0$ CoPt bulk ordered phase. We notice a surface segregation effect since the surface sublattices are well distinct from the bulk layers ones. Indeed, the surface stoichiometry is achieved before it is achieved in the bulk. At $c = 0.5 + \epsilon$, the γ and δ sublattices increase abruptly at the surface, whereas in the bulk, they increase more slowly to accommodate the variation of stoichiometry of the $L1_0$ phase up to the limit of the phase coexistence with the $L1_2$ $CoPt_3$ phase. This surface Pt enrichment is at the origin of a remarkable step in the segregation isotherm. This second plateau is associated to the last $c(2\times2)(111)$ surface structure, which consists in an ordered layer of the $L1_2$ $CoPt_3$ bulk phase occurring at the surface before that the $L1_2$ composition is

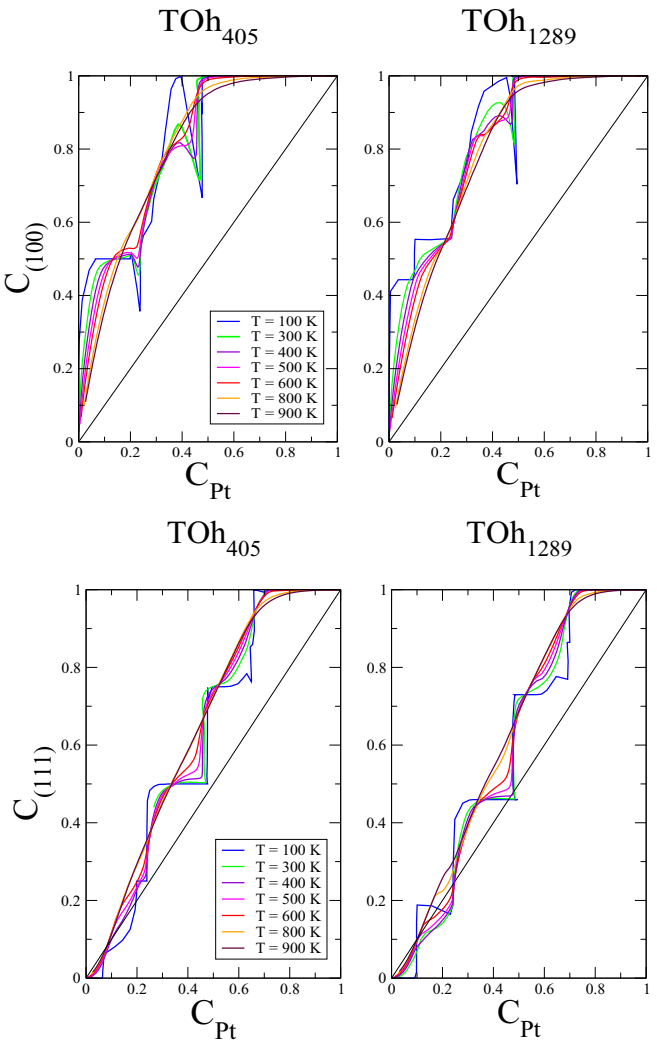

FIG. 11. (Color online) Segregation isotherms at various temperatures from 100 to 900 K for the (100) and the (111) facets of the clusters of 405 and 1289 atoms as a function of the cluster core Pt concentration.

reached in the bulk. So that the $c(2\times2)(111)$ surface structure is obtained already at the limit of the phase coexistence domain with the $L1_2$ phase, because of the surface segregation of Pt in the c_0^γ and c_0^δ surface sublattices. At the coexistence domain, the γ surface sublattice remains filled whereas the δ one goes down before to increase more strongly than the bulk δ ones. This is the last manifestation of the Pt surface segregation, which leads to a pure Pt surface on the $L1_2$ $CoPt_3$ bulk phase.

As a conclusion, for the (111) orientation, the bulk ordering controls the surface terminaison at the stoichiometry leading to the $c(2\times2)$ for the $L1_2$ Co_3Pt and $CoPt_3$ phases and the (2×1) for the CoPt $L1_0$ phase. Out-of-stoichiometry, Pt surface segregation modifies the surface composition as compared to the bulk in the ordered domains. For the overstoichiometric $L1_2$ Co_3Pt phase, surface segregation leads to the (2×1) surface structure before the $L1_0$ CoPt bulk phase domain. For the overstoichiometric $L1_0$ phase, the $c(2\times2)(111)$ surface structure occurs before the $L1_2$ $CoPt_3$ phase domain. Finally, the (111) surface becomes pure in Pt in the overstoichiometric $L1_2$ $CoPt_3$ phase, whereas each bulk layer have the $c(2\times2)(111)$ structure. So that here also, the surface displays a Pt segregation as compared to the bulk ordered phase, in good agreement with experimental results [16].

Experimentally, the $(2\times1)(111)$ surface structure has been observed by LEED and STM [17] for the Co_3Pt alloy. In our calculations, the first step in the isotherm is more abrupt when we lower the temperature so that at low temperature, the $(2\times1)(111)$ surface structure is indeed obtained because of surface segregation on the $L1_2$ Co_3Pt alloy, which is in good agreement with experimental results.

To conclude on the (100) and (111) surfaces at low temperature, the bulk ordering controls the overall surface composition on the two surface orientations, selecting the Pt-rich layer at the surface of the alloy. There are, however, surface segregation manifestations on the (111) surface for overstoichiometric compounds which lead to anticipate the surface composition and structure on the next ordered bulk phase (increasing the Pt content).

Concerning the equiatomic composition, there is no experimental comparison, however *ab initio* calculations [64] showed that the Pt covered $L1_1$ (111) surface presents a particularly low surface energy, possibly sufficient to overcompensate the energy cost of the $L1_1$ structure as compared to the $L1_0$ one, to stabilize the core/shell icosahedral structure in equiatomic nanoparticles [48,49].

V. TBIM Co-Pt NANOALLOYS

The segregation isotherms have been calculated on truncated octahedra (TOh) of 405 and 1289 atoms in a semigrand canonical ensemble. The truncated octahedron is the equilibrium cluster shape with the fcc structure. We consider two different sizes in order to study possible size effects. The

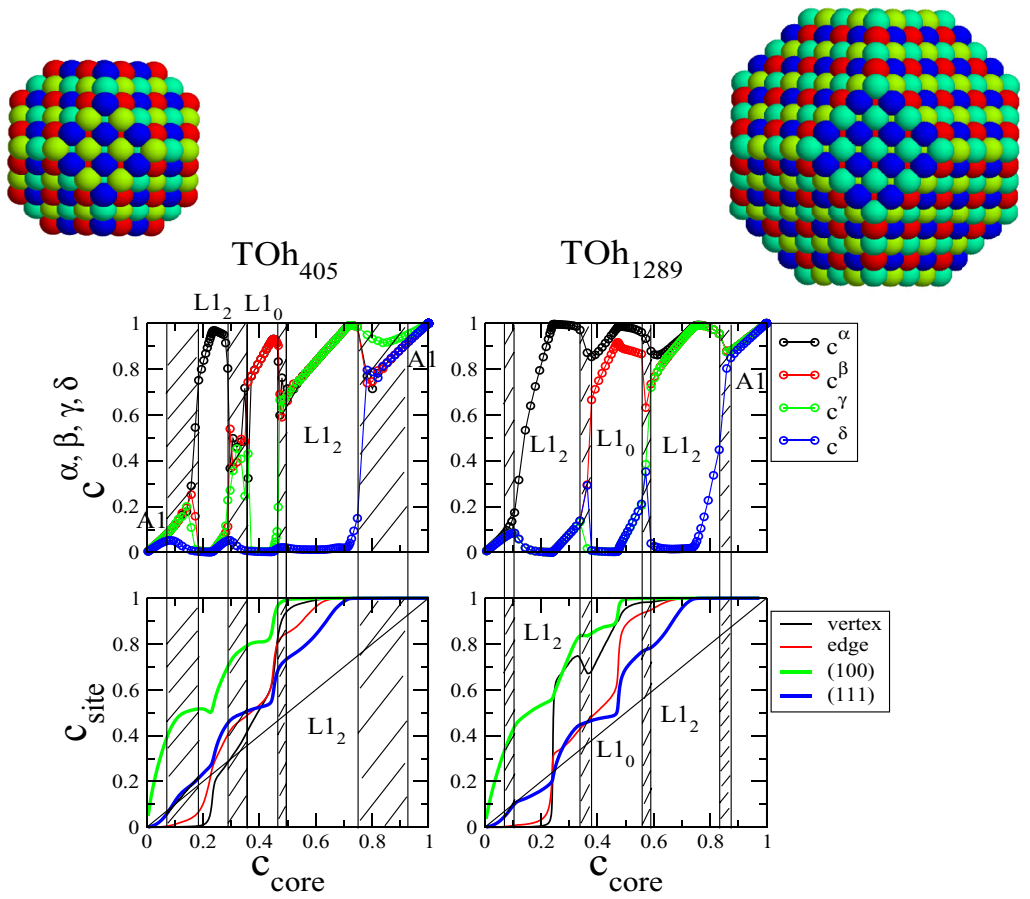

FIG. 12. (Color online) Sublattice occupation ($c^{\alpha,\beta,\gamma,\delta}$) and segregation isotherms (c_{site}) at 500 K for the 405 and 1289 atoms TOh clusters illustrated on top with the color corresponding to the four sublattices as defined in the bulk.

1289-atoms TOh is illustrated in Fig. 7 where the vertices, edges, (100) and (111) facets are distinguished by the same color as in their segregation curves. At high temperature (1200 K, Fig. 7), we noticed there is a significant Pt segregation on the (100) facets, mainly due to size mismatch effect as for the infinite surfaces. The (100) and (111) facets segregations are similar to the (100) and (111) infinite surfaces, respectively.

By lowering the temperature down to 100 K, we can see in Fig. 11 that the segregation isotherms on facets of the two cluster sizes become nonmonotonic. They display plateaus or cusp, which can be associated to the ordering of the clusters at low temperature.

The ordering of the clusters is illustrated in Fig. 12 where we can observe, by considering the occupation of the corresponding sublattice, that the cores of the two clusters of different size are ordered as in the bulk alloy. This is a nice verification that the cluster is well ordered at a temperature which is not so low, i.e., 500 K. But this is also a temperature allowing to get rid of the intermediate ordered phases found in the bulk below 500 K. By the way, we can notice that the 405-atom cluster core, in the coexistence domain between the $L1_2$ and $L1_0$ phase, is rather disordered. We also notice that for this small size, the ordered phase domains are much more asymmetric than in the largest size where the domain boundaries look like the ones in the bulk at the same temperature.

With the segregation isotherms at 500 K (Fig. 12), we get a first description of the overall segregation tendency on the clusters. It is worth to point out that in this figure and in the following we plot the core concentration in Pt instead of the global concentration. We will see at the end how it can be sensible since the cluster is a finite object so that the nominal concentration in a cluster is divided between its surface and its core. However, we would like first to compare the segregation isotherms to the one obtained in the infinite surfaces, for which there is an infinite reservoir corresponding to the nominal concentration of the alloy.

In Fig. 13, we plotted the segregation isotherms of the facets of the clusters and the one of the infinite surfaces to be compared. The comparison is very good in the case of the (111) facets for which we recall that the (111) surface presents essentially three different superstructures at the surface, corresponding to the three stoichiometric ordered phases Co_3Pt, CoPt, and $CoPt_3$, and a pure Pt surface layer for the overstoichiometric $CoPt_3$ phase. This is almost what appears in the clusters except a slight shift for the clusters which have the tendency to start the steps at lower concentrations than in the infinite system, especially in the Pt-rich domain. This is due to the finite size effect of the cluster since, on the one hand, the ordered $CoPt_3$ phase in the 405-atom cluster is shifted to lower concentrations and, on the other hand, the surface of the clusters is pure in Pt for core concentration of 70%, whereas it occurs at the stoichiometry of the $CoPt_3$ phase (i.e., 75%) for the (111) surface.

The comparison is less simple in the (100) orientation where we observe two main differences. At low concentration of Pt, the (100) facet segregation is higher than on the (100) surface, reaching sooner the equiconcentration at the facets (forming a plateau) than for the surface. Then, before the CoPt $L1_0$ phase, the segregation on the (100) facets goes through a maximum,

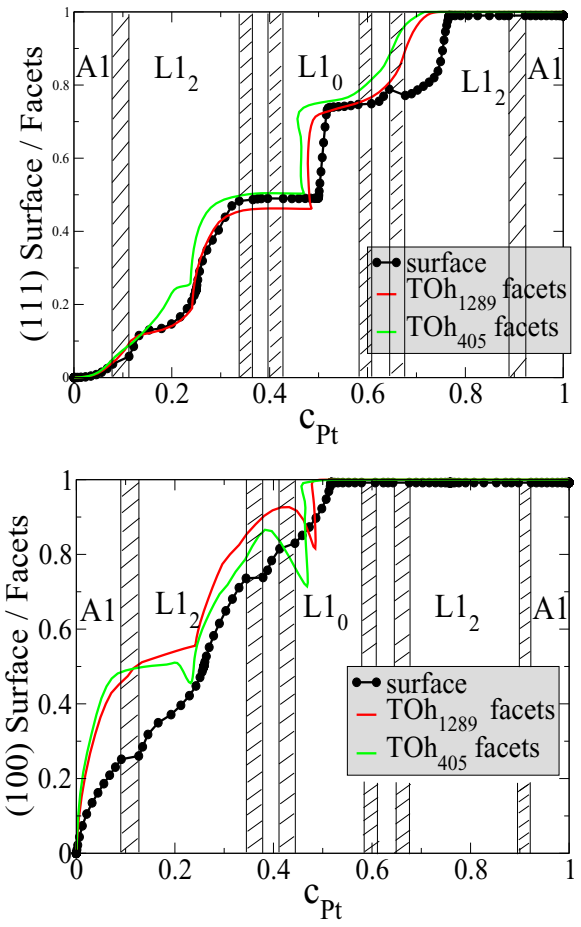

FIG. 13. (Color online) (111) and (100) facets segregation isotherms of the TOh_{405} and TOh_{1289} as compared to the infinite equivalent surfaces at 300 K. In the case of the clusters, the c_{Pt} concentration is the concentration of Pt in the core of the clusters to get a better comparison with the infinite surfaces.

then decreases a little before to increase abruptly around the equiconcentration to form pure (100) Pt facets. To understand these variations in the (100) facets segregation isotherms, we have to distinguish the (100) facets as a function of their orientation in the space (Fig. 14) because their composition can vary from one orientation to the other in the $L1_0$ or $L1_2$ phase. This has to be correlated with the different variants existing in the bulk phases. In the $L1_0$ bulk fragment, there are two pure (100) facets along the "z" axis, chosen as the axis along which there is the alternance of pure planes, and four mixed lateral (100) facets in the "x" and "y" directions. In the $L1_2$ bulk fragment and by optimizing the Pt concentration at the surface, the facets are all mixed except for the TOh_{405}. On the isotherms (Fig. 14), we can see that the concentration in each direction is equal except around 25% in Pt for the TOh_{405} and around the equiconcentration for the two sizes. In the last case, the (001) facets in the z direction are almost filled by Pt atoms, whereas the other lateral ones are almost mixed. These configurations are illustrated on the equilibrated clusters at 300 K by the $Co_{197}Pt_{208}$ and $Co_{655}Pt_{634}$ structures and can be compared to the perfect $L1_0$ phase as if the cluster remained as a fragment of the bulk ordered alloy. This is a signature of

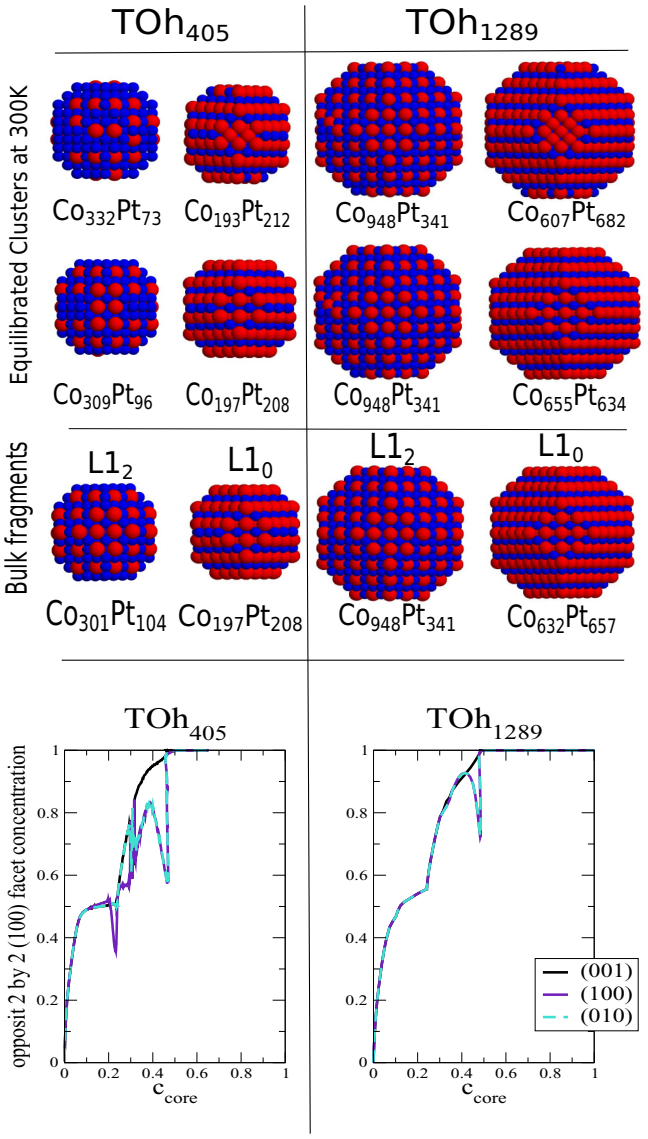

FIG. 14. (Color online) Snapshots of the TOh_{405} and TOh_{1289} around Co_3Pt and CoPt compositions at 300 K (first and second lines) as compared to the bulk $L1_2$ and $L1_0$ phase fragments in the third line. Segregation isotherms at 300 K of two opposite (100) facets taken two by two, following the three orientations: (100), (010), and (001) for the 405 and 1289 atoms TOh clusters. Co atoms are smaller and in blue, Pt atoms are larger and in red.

a strong tendency to order in this system, without frustration by segregation effects. However, out of this stoichiometry, Pt surface segregation tends to form pure (100) facets, as in the infinite surface, keeping almost the same core concentration but increasing the Pt concentration on the facets. This leads to an out-of-stoichiometry $L1_0$ ordered phase with almost pure (100) facets as illustrated by the $Co_{193}Pt_{212}$ and $Co_{607}Pt_{682}$ structures. This results in a competition between the core ordering and the surface segregation.

In the $L1_2$ Co_3Pt ordered phase, things are more subtle than in the $L1_0$ phase since they can depend on the truncation of the octahedron. In the 1289-atom TOh, the (111) facets are perfectly hexagonal (with equal edges) so that all the facets

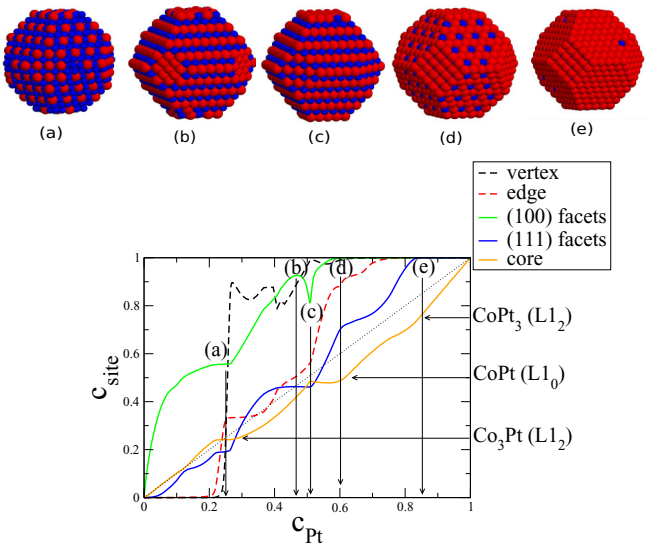

FIG. 15. (Color online) Segregation isotherms at 300 K for the 1289 atoms TOh cluster as a function of the nominal Pt concentration in the cluster and illustrations of the cluster configurations at different Pt concentrations: $c_{Pt} = 0.25$ (a), 0.46 (b), 0.50 (c), 0.60 (d), and 0.85 (e). Co atoms are smaller and in blue, Pt atoms are larger and in red.

are equivalent with the $c(2\times2)$ superstructure as in the infinite surfaces, without any segregation or ordering frustration. The equilibrated clusters adopt the same configuration as the bulk fragment ($Co_{948}Pt_{341}$). This is no more the case for the 405-atom TOh where the (111) facets have edges with four atoms and edges with three atoms leading to inequivalent (100) facets: two of the six facets are pure Co in the bulk $L1_2$ fragment ($Co_{301}Pt_{104}$), which represents a frustration for the Pt segregation. As a result, the cluster displays two different configurations depending on the stoichiometry. The one with less than 20% of Pt presents only mixed (100) facets ($Co_{332}Pt_{73}$) but stacking faults in the alternance of the pure and mixed planes, which represents an ordering frustration. The other one with almost 25% of Pt ($Co_{309}Pt_{96}$) is almost similar to the bulk $L1_2$ fragment so without frustration but we notice that the exact composition of the bulk $L1_2$ fragment is not achieved in average at 300 K.

Finally, we can summarize the results of the segregation versus ordering in the clusters by giving the surface segregation isotherms as a function of the nominal Pt concentration in the cluster and some snapshots on selected compositions (Fig. 15). We show on this graph the core concentration and point out the stoichiometry of the ordered phase to show their correspondence with the nominal concentration. The core is generally depleted in Pt to compensate the Pt surface segregation, except at low Pt concentration (below 25% of Pt) where the (100) Pt segregation is compensated by Co segregation on the edges and vertices. We draw five typical snapshots of the 1289 TOh cluster at room temperature. At the nominal concentration of 25% of Pt, the core is almost of the same composition as the nominal concentration and the cluster is ordered according to the $L1_2$ phase without segregation frustration (we recover the bulk $L1_2$ fragment as illustrated in Fig. 14). The (100) and the (111) facets display a $c(2\times2)$

substructure as in the case of their equivalent infinite surface and the vertex composition changes from Co pure to almost Pt pure. Around the equiconcentration, there is a second plateau of the core concentration corresponding to the $L1_0$ ordered phase and some variation of the (100) facets concentration as discussed before. Beyond the equiconcentration, the (100) facets are saturated in Pt and the (111) facets display the $c(2\times2)$ superstructure with a core ordered in the $L1_2$ phase. Beyond the composition of 85 % in Pt, the surface is a pure Pt shell and the core is a solid solution with Co impurities.

VI. CONCLUSIONS AND PERSPECTIVES

We presented a detailed theoretical study of the interplay in nanoalloys between surface segregation and core ordering using a simple tight-binding Ising model on a rigid lattice. Notably, within this model, we compare $Co_{1-c}Pt_c$ nanoalloys of 2 and 3 nm on all the range of concentration between pure Co to pure Pt clusters, with the Co-Pt bulk phase diagram and the segregation/ordering phenomena occurring at the (100) and (111) infinite surfaces. The complicated relation between the core ordering, where the clusters reproduce the bulk ordered phases, and the cluster surface segregation, where the facets are compared to the alloy surface segregation and superstructures, are analyzed in detail in order to put in evidence of original phenomena occurring in nanoclusters because of their finite size and typical geometry. We showed that the clusters get ordered in their core as in the bulk phase diagram but the smaller size presents an asymmetry as a function of the Pt concentration in the core, which is typically a finite size effect. The segregation on the (111) facets is the same as the one on the (111) surface, which means the facets present the $c(2\times2)$ and the (2×1) superstructures on a large range of stoichiometry. The (100) facets present either the mixed $c(2\times2)$ or the pure Pt configuration but their arrangement depends on the core ordering.

The main perspectives to such a study will be to overcome the rigid lattice assumption in order to take into account the effect of the atomic relaxations using the TB-SMA potential. We notably expect possible effects of the tetragonalization in the $L1_0$ phase on the facets segregation. This will also allow to study other symmetries as the decahedral or icosahedral ones.

ACKNOWLEDGMENTS

We acknowledge support from the French Research National Agency (ANR) through SimNanA Project No. ANR-08-NANO-003, the COST Action MP0903 and the French Institute for Development and Resources in Intensive Scientific Computing (IDRIS) (Grant 2013-096829).

[1] *Nanoalloys: From Theory to Application*, edited by R. Johnston and R. Ferrando, Faraday Discussion Vol. 138 (RSC Publishing, Cambridge, UK, 2008).
[2] R. Ferrando, J. Jellinek, and R. Johnston, Chem. Rev. **108**, 845 (2008).
[3] *Nanoalloys, Synthesis, Structure and Properties*, edited by D. Alloyeau, C. Mottet, and C. Ricolleau, Engineering Materials (Springer-Verlag, London, 2012).
[4] F. Ducastelle, in *Order and Phase Stability in Alloys*, edited by F. R. de Boer and D. G. Pettifor, Cohesion and Structure Vol. 3 (North-Holland, Elsevier Science, Amsterdam, Oxford, New York, Tokyo, 1991).
[5] *Surface Alloys, and Alloy Surfaces*, edited by D. P. Woodruff The Chemical Physics of Solid Surfaces, Vol. 10 (Elsevier, Amsterdam, 2002).
[6] P. Wynblatt and A. Landa, Comp. Mater. Sci. **15**, 250 (1999).
[7] A. V. Ruban and H. L. Skriver, Comp. Mater. Sci. **15**, 119 (1999).
[8] G. Tréglia, B. Legrand, F. Ducastelle, A. Saúl, C. Gallis, I. Meunier, C. Mottet, and A. Senhaji, Comp. Mater. Sci. **15**, 196 (1999).
[9] A. Christensen, A. V. Ruban, P. Stoltze, K. W. Jacobsen, H. L. Skriver, J. K. Norskov, and F. Besenbacher, Phys. Rev. B **56**, 5822 (1997).
[10] A. V. Ruban, H. L. Skriver, and J. K. Norskov, Phys. Rev. B **59**, 15990 (1999).
[11] M. Polak and L. Rubinovich, Surf. Sci. Rep. **38**, 127 (2000).
[12] U. Bardi, Rep. Prog. Phys. **57**, 939 (1994).
[13] Y. Gauthier, Surf. Rev. Lett. **3**, 1663 (1996).
[14] U. Bardi, A. Atrei, P. N. Ross, E. Zanazzi, and G. Rovida, Surf. Sci. **211–212**, 441 (1989).
[15] U. Bardi, A. Atrei, E. Zanazzi, G. Rovida, and P. N. Ross, Vacuum **41**, 437 (1990).
[16] Y. Gauthier, R. Baudoing-Savois, J. M. Bugnard, U. Bardi, and A. Atrei, Surf. Sci. **276**, 1 (1992).
[17] Y. Gauthier, R. Baudoing-Savois, J. Bugnard, W. Hebenstreit, M. Schmid, and P. Varga, Surf. Sci. **466**, 155 (2000).
[18] Y. Gauthier, P. Dolle, R. Baudoing-Savois, W. Hebenstreit, E. Platzgummer, M. Schmid, and P. Varga, Surf. Sci. **396**, 137 (1998).
[19] J. Bugnard, R. Baudoing-Savois, Y. Gauthier, and E. Hill, Surf. Sci. **281**, 62 (1993).
[20] J. Bugnard, Y. Gauthier, and R. Baudoing-Savois, Surf. Sci. **344**, 42 (1995).
[21] S. Sun, C. B. Murray, D. Weller, L. Folks, and A. Moser, Science **287**, 1989 (2000).
[22] T. O. Ely, C. Pan, C. Amiens, B. Chaudret, F. Dassenoy, P. Lecante, M.-J. Casanove, A. Mosset, M. Respaud, and J.-M. Broto, J. Phys. Chem. B **104**, 695 (2000).
[23] J. Park, M. G. Kim, Y.-W. Jun, J. S. Lee, W.-R. Lee, and J. Cheon, J. Am. Chem. Soc. **126**, 9072 (2004).
[24] P. Imperia, P. Andreazza, D. Schmitz, J. Penuelas, and C. Andreazza-Vignolle, J. Magn. Magn. Mater. **310**, 2417 (2007).
[25] J. Penuelas, C. Andreazza-Vignolle, P. Andreazza, A. Ouerghi, and N. Bouet, Surf. Sci. **602**, 545 (2008).
[26] J. Penuelas, P. Andreazza, C. Andreazza-Vignolle, H. C. N. Tolentino, M. De Santis, and C. Mottet, Phys. Rev. Lett. **100**, 115502 (2008).
[27] J. Penuelas, P. Andreazza, C. Andreazza-Vignolle, C. Mottet, M. De Santis, and H. C. N. Tolentino, Eur. Phys. J. Special Topics **167**, 19 (2009).

[28] P. Andreazza, C. Mottet, C. Andreazza-Vignolle, J. Penuelas, H. C. N. Tolentino, M. De Santis, R. Felici, and N. Bouet, Phys. Rev. B **82**, 155453 (2010).
[29] L. Favre, V. Dupuis, E. Bernstein, P. Mélinon, A. Préz, S. Stanescu, T. Epicier, J.-P. Simon, D. Babonneau, J.-M. Tonnerre, and J.-L. Hodeau, Phys. Rev. B **74**, 014439 (2006).
[30] S. Rohart, C. Raufast, L. Favre, E. Bernstein, E. Bonet, and V. Dupuis, Phys. Rev. B **74**, 104408 (2006).
[31] F. Tournus, A. Tamion, N. Blanc, A. Hannour, L. Bardotti, B. Prevel, P. Ohresser, E. Bonet, T. Epicier, and V. Dupuis, Phys. Rev. B **77**, 144411 (2008).
[32] A. Tamion, M. Hillenkamp, F. Tournus, E. Bonet, and V. Dupuis, Appl. Phys. Lett. **95**, 062503 (2009).
[33] D. Alloyeau, C. Ricolleau, C. Mottet, T. Oikawa, C. Langlois, Y. Le Bouar, and A. Loiseau, Nat. Mater. **8**, 940 (2009).
[34] D. Alloyeau, G. Prévot, Y. Le Bouar, T. Oikawa, C. Langlois, A. Loiseau, and C. Ricolleau, Phys. Rev. Lett. **105**, 255901 (2010).
[35] N. Blanc, F. Tournus, V. Dupuis, and T. Epicier, Phys. Rev. B **83**, 092403 (2011).
[36] J.-Y. Bigot, H. Kesserwan, V. Halt, O. Ersen, M. Moldovan, T. Kim, J.-T. Jang, and J. Cheon, Nano Lett. **12**, 1189 (2012).
[37] F. Tournus, K. Sato, T. Epicier, T. J. Kono, and V. Dupuis, Phys. Rev. Lett. **110**, 055501 (2013).
[38] N. Blanc, L. E. Diaz-Sánchez, A. Y. Ramos, F. Tournus, H. C. N. Tolentino, M. De Santis, O. Proux, A. Tamion, J. Tuaillon-Combes, L. Bardotti, O. Boisron, G. M. Pastor, and V. Dupuis, Phys. Rev. B **87**, 155412 (2013).
[39] D. Wang, H. Xin, R. Hovden, H. Wang, Y. Yu, D. A. Muller, F. DiSalvo, and H. D. Abruna, Nat. Mater. **12**, 81 (2012).
[40] M. V. Lebedeva, V. Pierron-Bohnes, C. Goyhenex, V. Papaefthimiou, S. Zafeiratos, R. R. Nazmutdinov, V. D. Costa, L. Zosiak, R. Kozubski, D. Muller, and E. R. Savinova, Electrochim. Acta **108**, 605 (2013).
[41] R. Chepulskii, J. Velev, and W. Butler, J. Appl. Phys. **97**, 10J311 (2005).
[42] R. V. Chepulskii and W. H. Butler, Phys. Rev. B **72**, 134205 (2005).
[43] M. Müller and K. Albe, Phys. Rev. B **72**, 094203 (2005).
[44] M. Müller, P. Erhart, and K. Albe, Phys. Rev. B **76**, 155412 (2007).
[45] P. Moskovkin and M. Hou, J. Alloys Compd. **434–435**, 550 (2007).
[46] B. Yang, M. Asta, O. Mryasov, T. Klemmer, and R. Chantrell, Scr. Mater. **53**, 417 (2005).
[47] B. Yang, M. Asta, O. Mryasov, T. Klemmer, and R. Chantrell, Acta Mater. **54**, 4201 (2006).
[48] M. E. Gruner, G. Rollmann, P. Entel, and M. Farle, Phys. Rev. Lett. **100**, 087203 (2008).
[49] M. Gruner and P. Entel, Int. J. Quant. Chem. **112**, 277 (2012).
[50] G. Rossi, R. Ferrando, and C. Mottet, Faraday Discuss. **138**, 193 (2008).
[51] R. V. Chepulskii and S. Curtarolo, Appl. Phys. Lett. **99**, 261902 (2011).
[52] R. V. Chepulskii and W. H. Butler, Phys. Rev. B **86**, 155401 (2012).
[53] F. Calvo and C. Mottet, Phys. Rev. B **84**, 035409 (2011).
[54] G. Tréglia, B. Legrand, and F. Ducastelle, Europhys. Lett. **7**, 575 (1988).
[55] A. Bieber, Thesis, Louis Pasteur University, Strasbourg, 1987.
[56] R. Hultgren, P. D. Desai, D. T. Hawkins, M. Gleiser, and K. K. Kelley, in *Selected Values of the Thermodynamic Properties of Binary Alloys* (American Society for Metals, Berkeley, Jossey-Bass Publishers, San Francisco, CA, 1981), p. 777.
[57] J. P. Perdew and Y. Wang, Phys. Rev. B **45**, 13244 (1992).
[58] P. E. Blöchl, Phys. Rev. B **50**, 17953 (1994).
[59] G. Kresse and D. Joubert, Phys. Rev. B **59**, 1758 (1999).
[60] V. Rosato, M. Guillopé, and B. Legrand, Phil. Mag. A **59**, 321 (1989).
[61] C. Dahmani, M. C. Cadeville, and V. Pierron-Bohnes, Acta Metall. **33**, 369 (1985).
[62] C. Leroux, M. C. Cadeville, V. Pierron-Bohnes, G. Inden, and F. Hinz, J. Phys. F: Met. Phys. **18**, 2033 (1988).
[63] C. Leroux, A. Loiseau, A. Broddin, and G. V. Tendeloo, Phil. Mag. B **64**, 57 (1991).
[64] A. Dannenberg, M. E. Gruner, A. Hucht, and P. Entel, Phys. Rev. B **80**, 245438 (2009).
[65] F. Lequien, J. Creuze, F. Berthier, I. Braems, and B. Legrand, Phys. Rev. B **78**, 075414 (2008).
[66] N. Metropolis, A. Metropolis, M. Rosenbluth, A. Teller, and E. Teller, J. Chem. Phys. **21**, 1087 (1953).
[67] J. M. Cowley, Phys. Rev. **77**, 669 (1950).
[68] G. Inden, Mater. Res. Soc. Symp. Proc. **19**, 175 (1983).
[69] Y. Le Bouar, A. Loiseau, and A. Finel, Phys. Rev. B **68**, 224203 (2003).
[70] M. Fèvre, C. Varvenne, A. Finel, and Y. Le Bouar, Phil. Mag. **93**, 1563 (2013).